


# Single-crystal studies and electronic structure investigation of the room-temperature semiconductor NaMnAs

Jiří Volný

*Department of Condensed Matter Physics, Faculty of Mathematics and Physics,  
Charles University, Ke Karlovu 5, Praha 2, CZ-12116, Czech Republic*

Kateřina Charvátová  and Martin Veis

*Institute of Physics of Charles University, Faculty of Mathematics and Physics, Ke Karlovu 5, Prague, CZ-12116 Czech Republic*

Václav Holý

*Department of Condensed Matter Physics, Faculty of Mathematics and Physics,  
Charles University, Ke Karlovu 5, Praha 2, CZ-12116, Czech Republic  
and Institute of Condensed Matter Physics, Faculty of Science, Masaryk University, Kotlářská 2, Brno CZ-61137, Czech Republic*

Martin Vondráček  and Jan Honolka 


*Institute of Physics, Academy of Sciences of the Czech Republic, Na Slovance 2, Praha 8, CZ-18221, Czech Republic*

Elen Duverger-Nédellec 

*Department of Condensed Matter Physics, Faculty of Mathematics and Physics,  
Charles University, Ke Karlovu 5, Praha 2, CZ-12116, Czech Republic  
and CNRS, ICMCB UMR5026, Bordeaux INP, University of Bordeaux, Pessac F-33600, France*

Jakub Schusser ,\* Sunil W. D'Souza, and Jan Minár

*New Technologies-Research Center, University of West Bohemia, Plzeň 3, CZ-30100, Czech Republic*

James M. Pientka 

*Department of Physics, St. Bonaventure University, St. Bonaventure, New York 14778, USA*

Alberto Marmodoro and Karel Výborný

*Institute of Physics, Academy of Science of the Czech Republic, Cukrovarnická 10, Praha 6, CZ-16253, Czech Republic*

Klára Uhlířová †

*Department of Condensed Matter Physics, Faculty of Mathematics and Physics,  
Charles University, Ke Karlovu 5, Praha CZ-12116, Czech Republic*



(Received 14 September 2021; revised 22 December 2021; accepted 31 January 2022; published 31 March 2022)

Synthesis of single-crystalline NaMnAs is reported, and we confirm its high quality by x-ray photoemission spectra. Magnetometry results are consistent with previous findings of antiferromagnetic order. The electronic structure was further studied using optical transmittance and by theoretical modeling using local-density approximation (LDA) extended to LDA +  $U$  for the purpose of determining the Heisenberg model parameters. Optical transmittance measurements confirm theoretical predictions that NaMnAs is a semiconductor. The Néel temperature was determined from temperature dependence of susceptibility, in agreement with our Monte Carlo simulations.

DOI: [10.1103/PhysRevB.105.125204](https://doi.org/10.1103/PhysRevB.105.125204)

## I. INTRODUCTION

Antiferromagnets (AFMs) are increasingly coming into the spotlight for spintronics applications [1–4]. In part, this

is motivated by robustness against stray magnetic fields for memory devices [5–7], thanks to compensation of magnetic moments. The aspect of linear spin-wave-dispersion close to the  $\Gamma$  point as opposed to the quadratic trend in ferromagnets [8] has also been considered for possible magnonics technology [9,10].

Whereas numerous AFM materials have been discovered up to now, for many of them, little is known beyond the bare fact that they are antiferromagnetic. One of the most

\*Experimentelle Physik VII and Würzburg-Dresden Cluster of Excellence ct.qmat, Universität Würzburg, Würzburg, Germany D-97074.

†klara@mag.mff.cuni.cz

intensely studied compounds in AFM spintronics [11,12], CuMnAs shows switching behavior in charge resistivity between binary [13] or multilevel [6] states, through the controlled application of electric current [14,15] or optical [16] pulses. Its tetragonal phase presents the additional benefits of above room-temperature antiferromagnetic ordering [17–23] as well as lack of lattice strain in the deposition over a GaP substrate.

On the other hand, similar to the other well-established example of  $\text{Mn}_2\text{Au}$ , CuMnAs presents no electronic band gap [24]. This feature would be highly desirable for further spintronics and magnonics technologies in which, for instance, lack of charge carriers have been predicted [25] and observed [26,27] to provide long-range magnons diffusion length due to the depopulated Stoner continuum.

Whereas the pursuit of better characterization of microscopic features and switching mechanisms in the most established AFMs continues and typically resorts to high quality samples prepared by molecular beam epitaxy [28–30], the search for other semiconducting AFMs has also carried on, taking advantage of the flexibility offered by bulk synthesis methods in exploring different compositions and lattice geometries.

Remaining within the  $\text{AMnX}$  family of alkaline metal/manganese-pnictide ternary compounds with a tetragonal nonsymmorphic space-group  $P4/nmm$  ( $\text{Cu}_2\text{Sb}$ -type structure), we recall the early work by Linowsky and Bronger (with  $A = \text{K}$  and  $X = \text{P, As}$ ) [31] Schuster and Achenbach (with  $A = \text{K, Na}$ , and  $X = \text{Sb, Bi, and P}$ ) [32], Achenbach and Schuster (with  $A = \text{Li and Na}$  and  $X = \text{P, As, Sb, and Bi}$ ) [33], Bronger *et al.* ( $X = \text{Na, Li, and K}$  and  $X = \text{P, As, Sb, and Bi}$ ) [34]. The later work showed that all these compounds order antiferromagnetically well above the room temperature. These materials have recently been rediscovered as potential antiferromagnetic semiconductors [28,35–39]. Here, we would like to focus on NaMnAs. Up to now only the crystal structure and magnetic structure by x-ray diffraction (XRD) and neutron diffraction, respectively, was reported on pulverised polycrystals [34]. It has been shown that it orders antiferromagnetically with magnetic moments aligned along the  $z$  axis and propagation vector  $k = [000]$ . The crystal and magnetic structure is presented in Fig. 1. The Néel temperature was estimated between 293 and 643 K; close to zero temperature, the Mn-magnetic moment was determined to be  $4.0 \mu_B/\text{Mn}$  [34].

We report on the high quality single-crystal growth of NaMnAs, confirm by optical transmission measurements its semiconducting nature and discuss various aspects of magnetic order both from experimental and theoretical point of view.

## II. SAMPLE GROWTH AND CHARACTERIZATION

The NaMnAs single crystals were grown similar to  $\text{Cu}_{1-x}\text{Mn}_{1+x}\text{As}$  using the flux method [40]. The single crystals were shiny flat rectangular plates ( $2 \times 2 \times 0.1 \text{ mm}^3$ ), which can be cleaved on the basal plane using a standard sticky tape. This suggests very weak bonds between the layers. A typical sample is shown in Fig. 2. The material is not stable on air. After a few minutes it becomes dark so most of

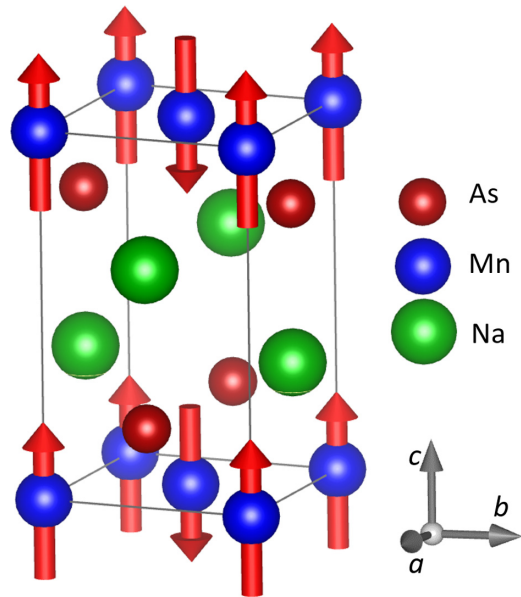


FIG. 1. Unit cell of NaMnAs with magnetic moment directions refined by Bronger *et al.* [34].

the manipulation has to be performed under protective atmosphere (see Supplemental Material [41]). It is rather typical for the flux method, that also other phases are grown; in this case MnAs crystals were formed during the synthesis. They form tiny needles which are often attached to the surface of NaMnAs crystals and are difficult to remove. This does not affect any spectroscopic measurements which are performed on impurity-free cleaved surfaces. They influence, however, other bulk measurements, such as magnetization (as discussed later).

### A. Composition and crystal quality

The composition and the crystal structure of selected single crystals have been determined by energy-dispersive x-ray

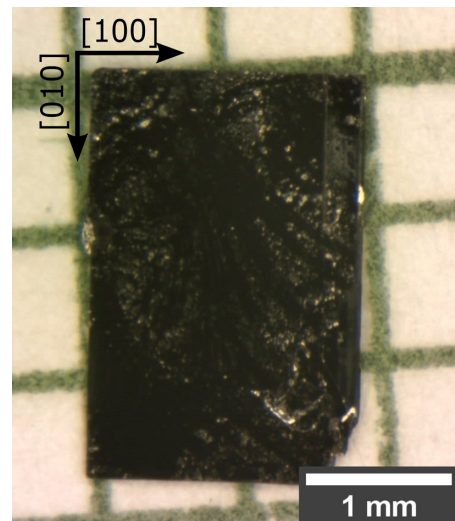


FIG. 2. Optical microscope image of typical NaMnAs single crystal. The sample thickness on the order of  $100 \mu\text{m}$ . The  $c$  axis is pointing perpendicular to the plane whereas  $a$  axes are parallel with the long edges of the sample.

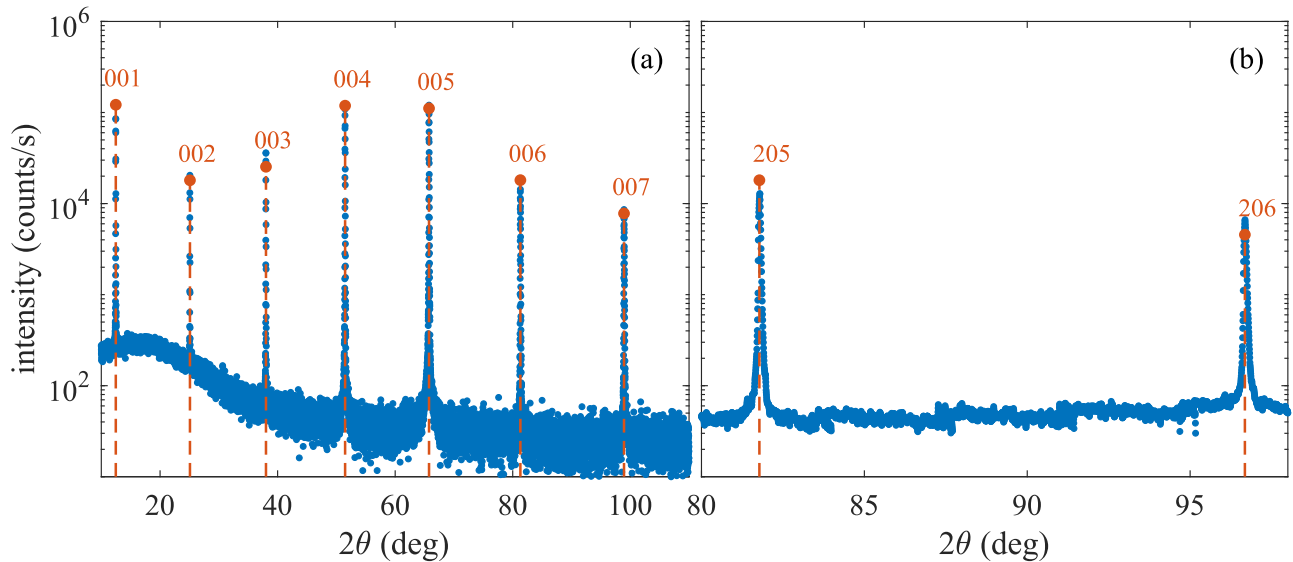


FIG. 3. (a) Symmetric  $2\theta/\omega$  scan of the (001) NaMnAs single crystals, and (b)  $Q_z$  scan across the (205) and (206) directions, respectively. Dashed lines represent the calculated diffraction intensities using the crystal structure from Ref. [34]. In the calculation we assumed an ideal kinematically diffracting crystal lattice.

spectroscopy (EDS) and by single-crystal XRD, respectively. EDS was performed using scanning electron microscope (SEM) equipped with an energy dispersive x-ray detector Bruker AXS which utilizes the ESPRIT software package (a nonstandard method with precision up to 1%). The as-grown samples were mounted on a SEM stub using carbon tape, freshly cleaved, and quickly installed into the SEM. The surfaces appear very flat and homogeneous with the stoichiometry:  $\text{Na}_{0.96(0.02)}\text{Mn}_{1.07(0.02)}\text{As}_{0.97(0.02)}$ , reproducible across several growth batches. High-resolution XRD using Rigaku Smartlab 45/200 in the parallel beam mode was performed at room temperature on an as-grown single crystal with the (001) planes parallel to the sample holder. The sample was preserved by kapton tape during the measurement. From the refined XRD peaks positions, a Cohen-Wagner plot provides the lattice parameters:  $a = b = 4.213 \pm 0.002$  and  $c = 7.0955 \pm 0.0005$  (Å). The crystal structure is presented in Fig. 1. The higher precision of the  $c$  parameter is due to the higher number of measured (001) diffraction peaks. Also the free  $z$  component of the  $2c$  atomic position was refined being 0.6675 and 0.2166 for Na and As atoms, respectively. The standard single-crystal diffraction collecting the full diffraction pattern was performed as well, however, the crystals exhibit a large degree of mosaicity, preventing proper crystal structure refinement as described in Supplemental Material [41] (for the used refinement method, see also Ref. [42]).

Figure 3 shows a symmetric  $2\theta/\omega$  scan of the (001) diffraction peaks. The peak width is limited by the resolution of the diffractometer, and it suggests excellent homogeneity of the crystals. Additionally, scans across the (205) and (206) directions were performed in order to determine the  $a$  lattice parameter.

### B. X-ray photoemission spectroscopy

The sample was investigated by x-ray photoemission spectroscopy (XPS) after a fresh cleave under UHV conditions.

Sodium, arsenic, and manganese shallow core levels (CLs) were probed using monochromatized Al  $K\alpha$  radiation ( $\hbar\omega = 1486.7$  eV), revealing depth-sensitive information about the sample composition and its homogeneity as discussed in the Supplemental Material [41]. In addition, details in the spectral line shape of Mn CLs allows an insight into the Mn  $3d$  shell configuration. The double-peak structure of the Mn  $2p_{3/2}$  CL is a typical multiplet splitting effect observed also in covalent bulk Mn oxides with oxidation states  $\text{Mn}^{2+}$  or  $\text{Mn}^{3+}$  and even  $\text{Mn}^{4+}$  [43].

The multiplet structure of the Mn  $2p$  CL in Fig. 4 can be fitted with five Voigt profiles (referred to as P1–P5) and a ranged Shirley background (a fit of similar quality can be achieved with a minimum of four peaks, where P2 and P3 merge to one broader peak). Energy positions, widths, and

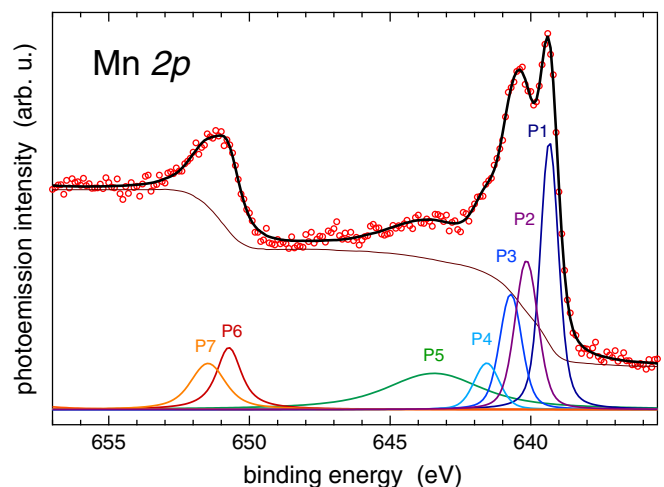


FIG. 4. XPS of the Mn  $2p$  core level. The fit (solid line) corresponds to seven Voigt profiles (P1–P7) assuming a ranged Shirley background. Parameters of peaks P1–P7 are given in Table I.

TABLE I. Peak energy positions, their full width at half maximum (FWHM), and total intensities of Voigt peaks  $P_1$ – $P_7$  in Fig. 4. For  $P_1$ – $P_4$ ,  $P_6$ , and  $P_7$  natural linewidths of 0.3 and 0.9 eV were assumed, respectively.

	$P_1$	$P_2$	$P_3$	$P_4$	$P_5$	$P_6$	$P_7$
Energy (eV)	639.3	640.2	640.7	641.6	643.4	650.7	651.5
FWHM (eV)	0.77	0.96	0.93	1.06	4.04	1.06	1.47
Area (a.u.)	183	124	93	42	151	71	67

intensities of the Voigt profiles are summarized in Table I. The fit structure resembles that of MnO where it is generally agreed that relativistic many-body effects dominate the spectral shape of Mn  $2p$  [44]: Angular momentum coupling of the  $2p$  core hole state and recoupling in the partially filled Mn  $d$ -shell state leads to a characteristic multiplet pattern consisting of four lines with  $J = 1$ – $4$  at the main  $2p_{3/2}$  peak and a satellite peak  $\approx 6$  eV higher in binding energy (BE) (peaks  $P_1$ – $P_5$ , respectively, in our case). Multiplet effects in the  $2p_{1/2}$  CL ( $P_6$  and  $P_7$ ) are of similar origin [45,46] but broadened due to super-Coster-Kronig decay processes, which limits the information on the Mn chemical state.

We briefly want to discuss nonlocal solid-state effects in NaMnAs, which have been, e.g., identified in MnO spectra [47]. Although the angular momentum coupling effect is mainly of local character (free  $\text{Mn}^{2+}$  atoms in the gas phase show a similar multiplet [44]) the relative intensities and energy positions of the peak structures  $P_1$ – $P_5$  are influenced by crystal fields, closed shell screening, or charge transfer (CT) effects. Although it is agreed that perturbations due to oxygen ligand orbitals do reshape Mn CLs in MnO [48], it was later concluded that CT configurations make, at most, minor contributions to spectral shapes in ionic Mn compounds [46,49]. We, therefore, believe that differences in the multiplet structure between MnO and NaMnAs are mostly due to changes in crystal symmetry of Mn in the ionized layered tetrahedral ( $\text{MnAs})^-$  environment [36] and the octahedral  $\text{MnO}_6$  environment in MnO [46,49]. A detailed analysis using a cluster model would be necessary, but it is beyond the scope of this paper.

We generally conclude that the object of our paper has been grown in the desired composition (without significant amounts of other phases, such as MnAs or manganese oxides) and relegate a more detailed analysis of the XPS for later investigations.

### C. Ultraviolet photoemission spectroscopy

The same device (as in the case of XPS) with a different photon excitation energy ( $\hbar\omega = 21.2$  eV, He I line) was used to obtain ultraviolet photoelectron spectroscopy (UPS) data shown in Fig. 5 covering BEs in the range of [2 eV,  $-0.5$  eV] measured in normal emission at a photon energy of 21.2 eV. The reference point  $E = 0$  eV corresponds to the Fermi level of the photoelectron spectroscopy analyzer. In semiconductors the position of the Fermi energy ( $E_F$ ) with respect to the valence-band maximum (VBM) is sensitive to defect states and possible surface band bending effects. Kraut *et al.* [50] described procedures to quantify defect induced shifts in  $E_F$

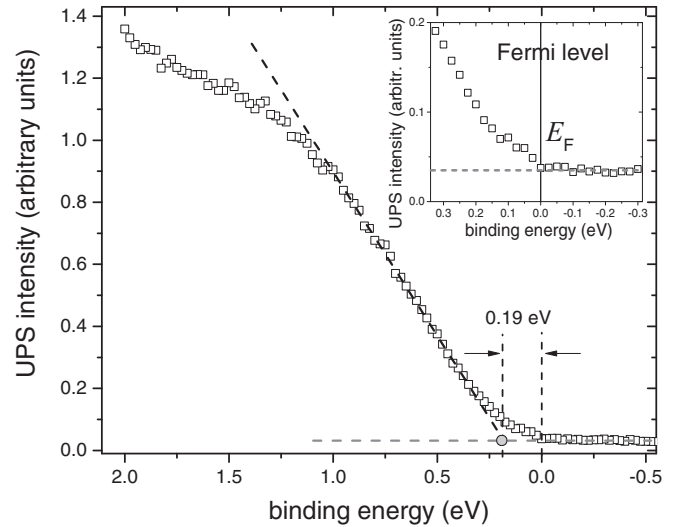


FIG. 5. UPS data covering the VBM region measured with a photon energy  $\hbar\omega = 21.2$  eV. The position of the VBM at 0.19 eV is estimated by the leading edge method (see the text). In the inset the signal intensity around  $E = 0$  (analyzer Fermi edge) is shown in detail.

and band bending in the semiconductor GaAs by referencing shallow CLs, such as  $E_{\text{Ga}3d}$  to the VBM value of  $E_{\text{VBM}}$ . Thereby values of  $E_{\text{VBM}}$  are estimated using the leading edge method, which approximates the density of states (DOS) by a tangential line at the maximum steepness of the VB edge.

In our case the tangential line of the dominant intensity suggests a VBM at  $E = 0.19$  eV. Looking more closely at the UPS intensity at lower BEs (see the inset in Fig. 5), it is evident that the intensity stretches all the way to  $E = 0$  and then disappears, suggesting a well-defined sample Fermi edge and that the Fermi level is intersecting the upper VB states. Therefore, we conclude that our sample is a  $p$ -type semiconductor.

### III. MAGNETIZATION MEASUREMENTS

In order to determine the Néel temperature  $T_N$  on NaMnAs single crystals, we have performed high-temperature magnetization measurements using the VSM oven option (Quantum Design physical property measurement system). A set of about 15 single crystals with total mass of 16 mg was placed in the sample holder and fixed by copper foil with the magnetic field oriented on the basal plane (see the Supplemental Material [41]). The temperature dependence of magnetization (under an applied magnetic field of 1 T) was measured in the range of 300–880 K.

We have observed, that the overall magnetic signal increases and slowly saturates upon repeating the heating cycles (Fig. 6). This is probably due to the fact that in vacuum and high-temperature conditions, the sample surface becomes Na deficient, and the larger amount of MnAs phase is grown, increasing the paramagnetic signal. This hypothesis is supported by XRD measurements of an as-grown and annealed piece of crystal (see the Supplemental Material [41]) where new MnAs peaks appeared after annealing the crystal at similar



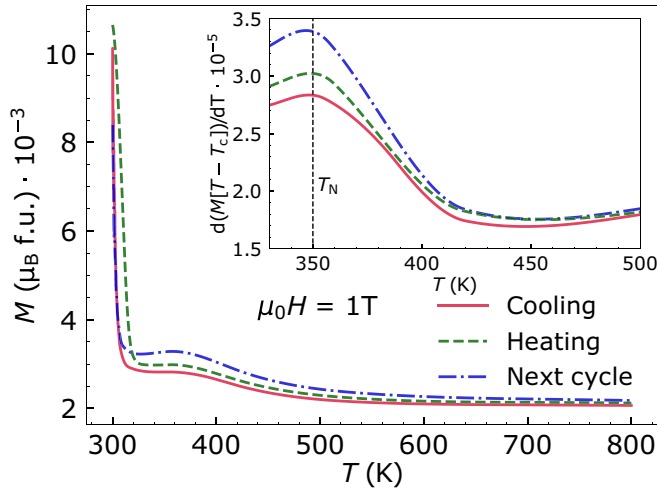


FIG. 6. Susceptibility measurements (temperature-dependent magnetization at  $B = 1$  T). The shift of maximum in the inset, upon thermal cycling, is likely an artifact of the signal-enhancement method.

conditions. MnAs in its hexagonal form orders ferromagnetically at around  $T_c = 315$  K with magnetic-field-dependent temperature hysteresis [51–53].

Magnetization isotherm plots (see Fig. 7) at 400 and 600 K show linear behavior without hysteresis, whereas the the isotherm at 350 K shows a weak paramagnetic contribution and a weak up-turn at high magnetic fields. At lower temperatures (not shown) a hysteresis can be seen connected to the presence of a small amount of ferromagnetic phase.

Considering the presence of such MnAs impurities, the magnetization measurement should be considered as partially qualitative. The value of  $T_N$  fits, however, in the expected range between 295 and 643 K reported by Bronger *et al.* [34]. The inset of Fig. 6 shows that once the Curie-Weiss background  $\propto 1/(T - T_c)$  is removed,  $T_N$  close to 350 K can be estimated.

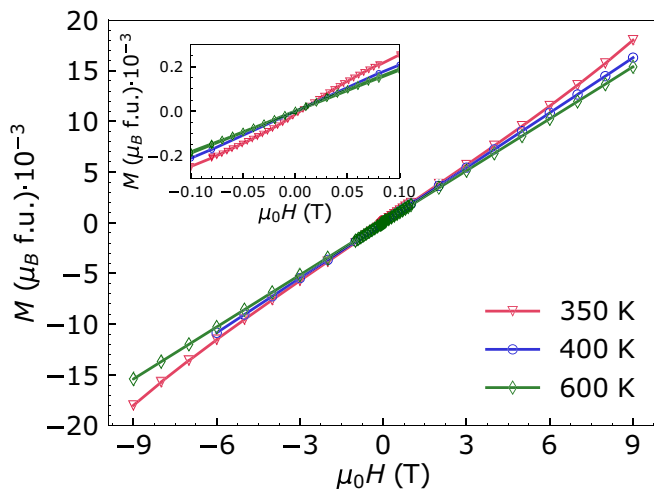


FIG. 7. Magnetization isotherm of NaMnAs single crystals with the magnetic field oriented on the basal plane.

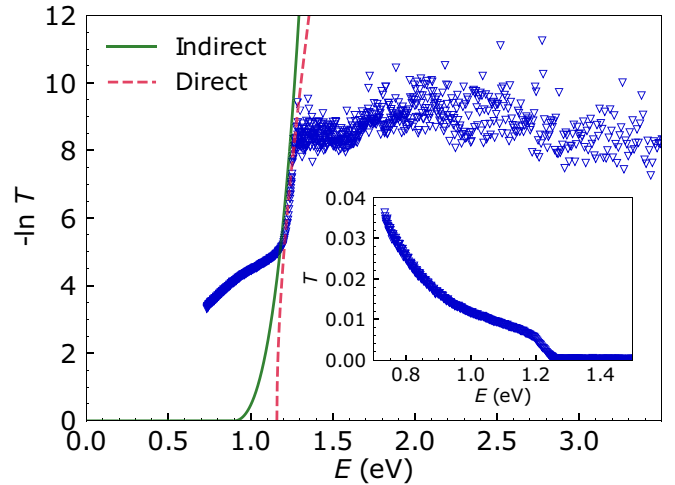


FIG. 8. The inset: The spectral dependence of the optical transmission  $T$ . The main plot: The same data replotted as  $-\ln T(E)$  fits in the interval of 1.2–1.4 eV by a direct (red, dashed) or indirect band-gap model allow to estimate the band gap.

#### IV. MEASUREMENTS OF THE OPTICAL GAP

Optical transmission measurements offer a straightforward means to prove the presence of a band gap. The measurements were performed using a Woollam RC2 Mueller matrix ellipsometer in the spectral range from 0.7 to 6 eV. The data were corrected for the baseline measurement without the sample in optical path, the resulting transmission data are shown in Fig. 8 on a logarithmic scale with the raw data in the inset. The higher level of noise above 1.26 eV is due to extremely low transmission where the detected light intensity is reaching the sensitivity limit of the equipment. A rapid decrease in transmission towards higher energies near 1.19 eV is a notable sign of the onset of interband transitions, giving the approximate estimation of the gap.

Given the definition of  $T(E) = I/I_0$ , a ratio of incoming and outgoing intensity of light at energy  $E = \hbar\omega$ , in terms of absorption coefficient  $\alpha$ , the sample width  $w$ , the imaginary part of complex permittivity  $\epsilon = \epsilon_1 + i\epsilon_2$  can easily be extracted from Fig. 8. We write

$$-\ln T(E) = w \frac{E}{\hbar c} \frac{\epsilon_2}{\sqrt{\epsilon_1}},$$

and fit the experimental data assuming  $\epsilon_2 \propto \sqrt{E - E_0}$  for a direct gap and  $\epsilon_2 \propto (E - E_0)^2$  for an indirect gap. The measurement clearly indicates that there is a band gap: an indirect (direct) band gap fit assuming  $\epsilon_1 = \text{const}$  yields the gap of 0.9 (1.16) eV. The absorption shoulder at lower energies may be ascribed to defect states inside the gap or twisting of the planes with respect to each other. As already discussed above, although the symmetric XRD scan presented in Fig. 3 suggest high quality of single crystal, the single-crystal diffraction showing the full reciprocal space shows on significant basal plane mosaicity, which can be a source of the low-temperature absorption shoulder. Another method, such as spectroscopic ellipsometry can provide wider information about the absorption edge and band structure of the material and will be the subject of our further studies of NaMnAs.

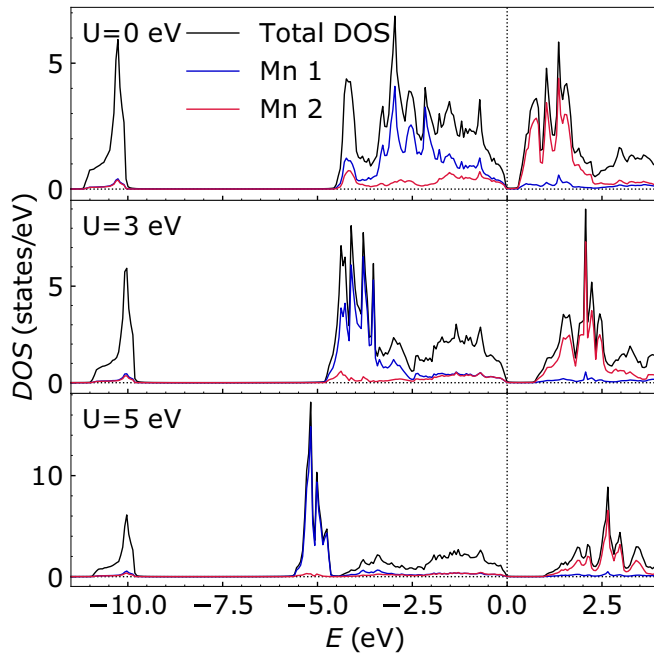


FIG. 9. Total spin-up and Mn-projected DOS from LDA +  $U$  calculations with  $U = 0, 3,$  and  $5$  eV (magnetic moments on Mn sites are 3.77, 4.27, and 4.51 Bohr magneton, respectively). Note that spin-down DOS is the same (and the Mn1 and Mn2 projected DOS swaps).

## V. THEORETICAL MODELING

### A. Electronic structure

Magnetic compounds containing manganese in the nominal  $3d^5$  configuration often share a generic electronic structure: Although the existence of the gap is optional, the anion-based bands provide a background for the spin-split Mn  $d$  states one of which (majority spin in the case of ferromagnets) is below, and the other above is above the Fermi level. Previous *ab initio* calculations [28,35] predicted that tetragonal XMnAs antiferromagnetic materials (where  $X$  is an alkali metal) do have a gap and, for example, CuMnAs is a metal with low DOS at the Fermi level ( $E_F$ ), see Fig. 3 in Ref. [20]. Given the well-documented [54] deficiencies of density functional theory (DFT) implementations,<sup>1</sup> such predictions need experimental confirmation.

In our DFT (optionally, DFT +  $U$  when the Hubbard term was included) calculations, we used lattice parameters from Ref. [35], namely,  $a_{lat} = b_{lat} = 4.200$ ,  $c_{lat} = 7.082$  Å, and sublattice origin at Wyckoff positions  $2c$ : (0, 0.5, 0.646),  $2a$ : (0, 0, 0) and  $2c$ : (0, 0.5, 0.215), respectively, for Na, Mn, and As atoms. We chose the local-density approximations (LDA) as our starting point for DFT. Apart from an undersized gap, a simple LDA calculation leads to Mn magnetic moments about 10% smaller than what is found experimentally ( $S_{Mn}^{exp} = 4.01$  Bohr magneton at low temperatures, see Table 2 in Ref. [34]). Regardless of the detailed implementation of

DFT +  $U$ , calculated  $S_{Mn}$  become larger when  $U$  increases. Such gradual changes can be seen in the DOS shown in Fig. 9. A compromise among several factors (magnetic moments, gap size, estimates of Néel temperature discussed in the next subsection) directed us to a value of  $U$  around 5 eV. On the experimental side, realistic magnitude of Mn magnetic moments [34] would suggest somewhat smaller  $U$ , but the final judgment should depend on a more direct quantity (such as Mn  $d$ -peak characteristics in UV photoemission spectroscopy). In the following, we use both LDA and LDA +  $U$  in the atomic sphere approximation as implemented within the spin-polarized relativistic Korringa-Kohn-Rostoker electronic structure package [55,56].

### B. Heisenberg parameters

Effective spin Hamiltonians allow to study finite-temperature properties of magnetic systems (such as NaMnAs) at a reasonable computational cost (see also the discussion in the Appendix). They use various parameters as input (for example, magnetic anisotropy may be accounted for or neglected, depending on the model complexity), but Heisenberg exchange parameters  $J_{ij}$  are always at their heart. These parameters quantify the coupling between magnetic moments on sites  $i, j$  and, as a matter of approximation, we identify Mn as the only magnetic atom (forming two sublattices) in NaMnAs. In our paper,  $J_{ij}$  are determined using the method of Ref. [57] i.e., starting from the perturbed (see the expression for  $\delta V_i$  in the Appendix) antiferromagnetic ground state (reflected in the  $\tau$  matrices, also discussed in the Appendix) and evaluating,

$$J_{ij} = \frac{(-1)^{\xi_{ij}}}{4\pi} \int_{-\infty}^{E_F} dE \text{Im Tr } \delta V_i \tau_{\uparrow}^{ij} \delta V_j \tau_{\downarrow}^{ji}. \quad (1)$$

Herewith, the complicated quantum-mechanical problem (crystal with many electrons) is mapped to a relatively simple lattice model of classical spins with pair interactions only. We offer further comments on this mapping, including the sign convention  $(-1)^{\xi_{ij}}$ , in the Appendix and here, we just state that once the magnetic part of the system energy is approximated by a model, such as Eq. (2), various thermodynamic quantities can be estimated using Monte Carlo (MC) simulation. For example, temperature-dependent magnetization can be extrapolated to zero and, thus, Néel temperature obtained. Alternatively, the same can be fitted to extract information beyond  $T_N$ , such as critical exponents (see the next subsection).

In Fig. 10, we show Heisenberg parameters obtained by Eq. (1) from an LDA +  $U$  zero-temperature calculation ( $U = 5$  and  $J = 0.68$  eV) plotted as a function of the distance between individual Mn atoms. This is a simplified representation of the situation created by an anisotropic crystal: The complete layout of  $J_{ij}$ 's in real space is shown in Fig. 12 (of the Appendix). It should be pointed out that the couplings are clearly dominated by the nearest-neighbor (NN) pairs within one plane of Mn atoms (both inter- and intrasublattice) and the next-nearest-neighbor  $J_{ij}$  are more than an order of magnitude smaller. The antiferromagnetic intersublattice NN coupling  $J_{ab}$  competes with the intrasublattice NN interaction. More distant pairs interact feebly and coupling between different layers is also weak. The NN in a different layer, i.e., shortest

<sup>1</sup>To be more precise, we mean fundamental shortcomings of some exchange-correlation kernels.

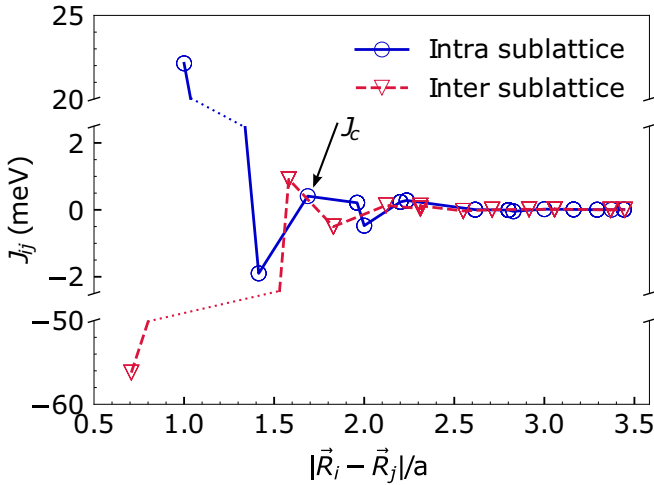


FIG. 10. Calculated Heisenberg exchange parameters  $J_{ij}$  plotted as a function of distance between Mn sites  $i$  and  $j$ . The arrow indicates  $J_{ij}$  corresponding to the coupling between nearest neighbors belonging to different layers.

interlayer coupling (corresponding to  $J_c$  and highlighted by an arrow in Fig. 10) belongs to the same magnetic sublattice and  $|J_c/J_{ab}| \sim 10^{-2}$ .

Comparing LDA to LDA +  $U$  calculations, we find that the coupling between Mn magnetic moments decreases with increasing  $U$ . However, this seems to be compensated by the enhancement of magnetic moments (see the discussion of Monte Carlo simulations in the next subsection). Zhou *et al.* noted that calculations (using a different method [58]) are robust with respect to the alternative choice of exchange-correlation functional (generalized gradient approximation and local spin-density approximation used in Ref. [35]), thanks to the overbinding artifact of the latter canceling out in

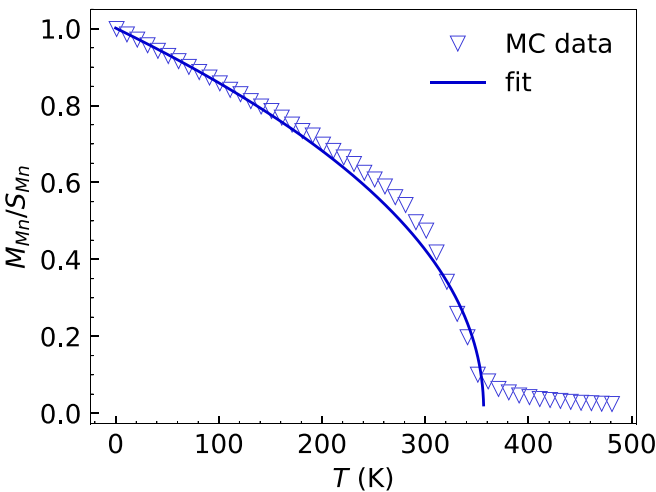


FIG. 11. Normalized temperature-dependent average magnetic moment on one Mn sublattice (blue triangles) from Monte Carlo simulations (see the text). The fit (also described in text) allows to more easily read off the Néel temperature  $T_N$  (to be compared with the peak position in Fig. 6).

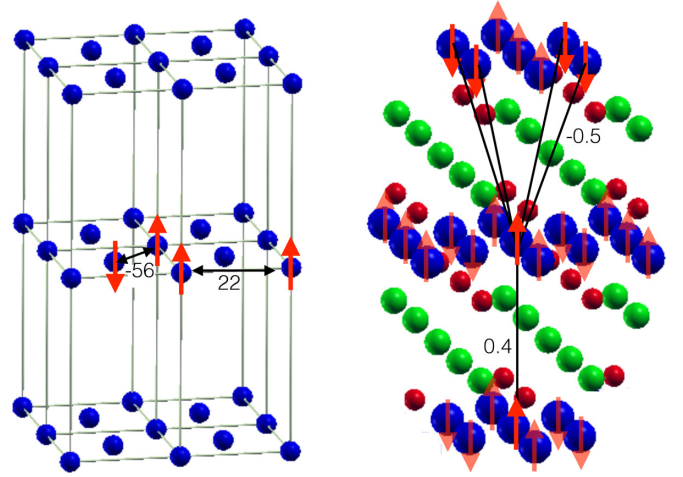


FIG. 12. Visualization of Heisenberg exchange parameters  $J_{ij}$  in the direct space. The two strongest couplings are shown on the left (here, only Mn atoms are displayed) and the two strongest *interlayer* couplings are shown on the right. Note that among the latter, there is only one NN but four next-NNs. Energies are given in meV.

taking the difference. The reduced dimensionality of the magnetic interactions, mainly confined to the (001) Mn planes, can explain the much smaller ordering temperature revealed by experiments and by Monte Carlo simulation as opposed to cruder early estimates in terms of total energy difference alone or mean-field theory calculations.

### C. Néel temperature

Several approaches to theoretically estimate the ordering temperature are possible, and their short review is given in the Appendix. Here, we employ MC calculations [59] as implemented the Uppsala Atomistic Spin Dynamics UPPASD code [60] whose input are the  $J_{ij}$  parameters discussed in the previous subsection.

Zero-temperature magnetization on sublattice  $i$  is taken to be  $S_{Mn}\bar{m}_i$  where  $|\bar{m}_i| = 1$  (i.e., we only consider Mn atoms). Temperature-dependent  $M_{Mn}/S_{Mn}$  for NaMnAs shown in Fig. 11 is fitted using  $t^\beta$  where [61]  $t = 1 - T/T_N$  and  $\beta$  is the critical exponent. It suggests that ordering temperature is slightly above 350 K. This agrees well with experimental data shown in Fig. 6. The lower  $T_N$  of NaMnAs with respect to CuMnAs can be tentatively understood as a consequence of different effective coordination or local environment for the Mn atoms within the two materials. Although for manganese pnictide CuMnAs the transition metal (Mn atoms) is arranged in a rumpled geometry ( $2c$  positions in the CuSb<sub>2</sub>-type structure), in NaMnAs the manganese creates flat planes ( $2a$  positions of the CuSb<sub>2</sub>-type structure). In combination with the fairly short-ranged  $J_{ij}$ s which present only weak coupling across such planes, the magnetic Hamiltonian becomes effectively two dimensional; Mermin-Wagner theorem [62] does not apply, however, given the sizable magnetic anisotropy (discussed in the Supplemental Material [41]).

## VI. CONCLUSIONS

We have prepared the room-temperature antiferromagnet NaMnAs for the first time in the single-crystalline form. The single crystals have a layered tetragonal structure and can be easily cleaved within the basal plane; they are, in general, very soft. The magnetization measurement showed the Néel temperature to be 350 K which is in agreement with *ab initio* calculations and falls within the temperature range suggested by previous neutron-diffraction experiments on polycrystals [34]. Using ultraviolet photoemission spectroscopy and optical transmittivity measurements we showed that NaMnAs is a *p*-type semiconductor with a band gap between 0.9 and 1.16 eV depending on whether the band gap is direct or indirect, respectively. The detailed studies of the type of band gap and band structure, in general, will be subject of our further work as NaMnAs seems a promising material for fabrication of functional devices [1,11].

## ACKNOWLEDGMENTS

We gratefully acknowledge computational resources from the Information Technology for Innovation (IT4I) Grants: Grants No. OPEN-19-45, No. OPEN-20-12 and from the Project “e-Infrastruktura CZ” (Grant No. e-INFRA LM2018140) provided within the Program Projects of Large Research, Development and Innovations Infrastructures, Operational Program Research, Development and Education financed by European Structural and Investment Funds and the Czech Ministry of Education, Youth and Sports (Project MAT-FUN Project No. CZ.02.1.01/0.0/0.0/15\_003/0000487). Single-crystal growth and characterization were performed in MGML, which is supported within the Program of Czech Research Infrastructures (Project No. LM2018096). M.V. and J.H. acknowledge support from the Czech Ministry of Education, Youth and Sports (Project No. SOLID21-CZ.02.1.01/0.0/0.0/16\_019/0000760). J.M. acknowledges support from GAČR Project No. 2018725S. The work of A.M. was supported via the Czech Science Foundation grant EXPRO No. 19-28375X.

## APPENDIX: THEORETICAL APPROACHES TO CRITICAL TEMPERATURE ESTIMATION

Spin Hamiltonians (see also Sec. V C) such as

$$E = -\frac{1}{2}S_{\text{Mn}}^2 \sum_{i \neq j} \tilde{J}_{ij} \vec{m}_i \cdot \vec{m}_j \quad (\text{A1})$$

can be understood as effective models of an otherwise complicated and computationally demanding description at

the electronic structure level (of crystalline solid exhibiting magnetic order). Such effective models capture the part of system’s total energy related to atomic magnetism, and their parameters can either be obtained by fitting to experimental data or as nicely summarized in the introduction of Ref. [63], using *ab initio* calculations as an input. We will also refer to Sec. II of Ref. [64] below and offer further comments on Eq. (2) in the Supplemental Material [41].

The easiest (and also very popular) way to estimate ordering temperature of an AFM system is to consider its hypothetical FM counterpart and use the energy difference [28] in combination with the assumption that only nearest-neighbor interactions are important. This crude approach can be refined by mapping the total energy difference onto the Heisenberg Hamiltonian, and estimating coupling between the nearest neighbors, second-nearest neighbors and further away through comparison of distinct magnetic orderings (see, for example, part B2 of Ref. [64]).

A better approach is to calculate the Heisenberg parameters by expressing the valence-band energy [66] as a function of magnetic moment directions. Assuming a certain ground state, Eq. (2) is exact up to second order in angles (tilt from the position corresponding to the ground state) of any pair of magnetic moments. Procedure [57] yielding Eq. (1) is implemented in our SPR-KKR calculations where the sign  $(-1)^{\xi_{ij}}$  is positive (negative) for atoms on sites  $i, j$  having the parallel (antiparallel) magnetic moment, i.e., belonging to the same (different) magnetic sublattices (we only consider Mn atoms in Fig. 10). In that formula,  $\delta V_i$  is derived from a Taylor expansion in terms of the rotation of the  $i$ th magnetic moment which gives

$$\delta V_i = t_{i\uparrow}^{-1} - t_{i\downarrow}^{-1}, \quad (\text{A2})$$

where the single-site scattering matrices [65]  $t_i$  can also be used to express  $\tau$  in Eq. (1), see Sec. 4 in Ref. [66]. Thus, calculated parameters  $J_{ij}$  can either be used at the mean-field level (see, for example, part C2 of Ref. [64]) or, in a more elaborate approach, Monte Carlo simulation can be performed to estimate the averaged sum of magnetic moments and the ordering temperature.

We replot the Heisenberg model parameters shown in Fig. 10 in the full three-dimensional representation: Fig. 12 highlights the difference between intra- and interlayer couplings. Although the antiferromagnetic order within the Mn plane is stabilized by a strong intersublattice  $J_{ab} < 0$ , couplings between the two layers are about two orders of magnitude weaker. Discussion of magnetic order continues in the Supplemental Material ([41] Fig. S8) and here we just note that the doubled magnetic unit cell in some materials similar to NaMnAs (such as KMnAs [34]) is probably related to slightly different values of interlayer couplings.

[1] T. Jungwirth, J. Wunderlich, V. Novák, K. Olejník, B. L. Gallagher, R. P. Campion, K. W. Edmonds, A. W. Rushforth, A. J. Ferguson, and P. Nemeč, Spin-dependent phenomena and device concepts explored in (Ga,Mn)As, *Rev. Mod. Phys.* **86**, 855 (2014).

[2] X. Marti, I. Fina, and T. Jungwirth, Prospect for antiferromagnetic spintronics, *IEEE Trans. Magn.* **51**, 2900104 (2015).

[3] O. Gomonay, T. Jungwirth, and J. Sinova, Concepts of antiferromagnetic spintronics, *Phys. Status Solidi RRL* **11**, 1700022 (2017).



- [4] M. B. Jungfleisch, W. Zhang, and A. Hoffmann, Perspectives of antiferromagnetic spintronics, *Phys. Lett. A* **382**, 865 (2018).
- [5] X. Marti, I. Fina, C. Frontera, J. Liu, P. Wadley, Q. He, R. Paull, J. Clarkson, J. Kudrnovský, I. Turek, J. Kuneš, D. Yi, J.-H. Chu, C. Nelson, L. You, E. Arenholz, S. Salahuddin, J. Fontcuberta, T. Jungwirth, and R. Ramesh, Room-temperature antiferromagnetic memory resistor, *Nature Mater.* **13**, 367 (2014).
- [6] K. Olejník, V. Schuler, X. Marti, V. Novák, Z. Kašpar, P. Wadley, R. P. Champion, K. W. Edmonds, B. L. Gallagher, J. Garces, M. Baumgartner, P. Gambardella, and T. Jungwirth, Antiferromagnetic CuMnAs multi-level memory cell with microelectronic compatibility, *Nat. Commun.* **8**, 15434 (2017).
- [7] P. Wadley, S. Reimers, M. J. Grzybowski, C. Andrews, M. Wang, J. S. Chauhan, B. L. Gallagher, R. P. Champion, K. W. Edmonds, S. S. Dhesi, F. Maccherozzi, V. Novak, J. Wunderlich, and T. Jungwirth, Current polarity-dependent manipulation of antiferromagnetic domains, *Nat. Nanotechnol.* **13**, 362 (2018).
- [8] S. M. Rezende, A. Azevedo, and R. L. Rodríguez-Suárez, Introduction to antiferromagnetic magnons, *J. Appl. Phys.* **126**, 151101 (2019).
- [9] V. V. Kruglyak, S. O. Demokritov, and D. Grundler, Magnonics, *J. Phys. D: Appl. Phys.* **43**, 264001 (2010).
- [10] A. V. Chumak and H. Schultheiss, Magnonics: Spin waves connecting charges, spins and photons, *J. Phys. D: Appl. Phys.* **50**, 300201 (2017).
- [11] V. Baltz, A. Manchon, M. Tsoi, T. Moriyama, T. Ono, and Y. Tserkovnyak, Antiferromagnetic spintronics, *Rev. Mod. Phys.* **90**, 015005 (2018).
- [12] T. Jungwirth, J. Sinova, A. Manchon, X. Marti, J. Wunderlich, and C. Felser, The multiple directions of antiferromagnetic spintronics, *Nat. Phys.* **14**, 200 (2018).
- [13] P. Wadley, B. Howells, J. Zelezny, C. Andrews, V. Hills, R. Champion, V. Novak, K. Olejník, F. Maccherozzi, S. Dhesi, S. Martín, T. Wagner, J. Wunderlich, F. Freimuth, Y. Mokrousov, J. Kune, J. Chauhan, M. Grzybowski, A. Rushforth, K. Edmonds *et al.*, Electrical switching of an antiferromagnet, *Science* **351**, 587 (2016).
- [14] M. J. Grzybowski, P. Wadley, K. W. Edmonds, R. Beardsley, V. Hills, R. P. Champion, B. L. Gallagher, J. S. Chauhan, V. Novak, T. Jungwirth, F. Maccherozzi, and S. S. Dhesi, Imaging Current-Induced Switching of Antiferromagnetic Domains in CuMnAs, *Phys. Rev. Lett.* **118**, 057701 (2017).
- [15] P. Wadley and K. W. Edmonds, Spin switching in antiferromagnets using Néel-order spin-orbit torques, *Chin. Phys. B* **27**, (2018).
- [16] Z. Kašpar, M. Surýnek, J. Zubáč, F. Krizek, V. Novák, R. P. Champion, M. S. Wörmle, P. Gambardella, X. Marti, P. Němec, K. W. Edmonds, S. Reimers, O. J. Amin, F. Maccherozzi, S. S. Dhesi, P. Wadley, J. Wunderlich, K. Olejník, and T. Jungwirth, *Nat. Electronics* **4**, 30 (2021).
- [17] F. Máca, J. Mašek, O. Stelmakhovych, X. Martí, H. Reichlová, K. Uhlířová, P. Beran, P. Wadley, V. Novák, and T. Jungwirth, Room-temperature antiferromagnetism in CuMnAs, *J. Magn. Mater.* **324**, 1606 (2012).
- [18] P. Wadley, V. Hills, M. Shahedkhah, K. Edmonds, R. Champion, V. Novák, B. Ouladdiaf, D. Khalyavin, S. Langridge, V. Saidl, P. Nemeč, A. Rushforth, B. Gallagher, S. Dhesi, F. Maccherozzi, J. Železný, and T. Jungwirth, Antiferromagnetic structure in thin films of tetragonal CuMnAs, *Sci. Rep.* **5**, 17079 (2015).
- [19] F. Máca, J. Kudrnovský, V. Drchal, K. Carva, P. Baláž, and I. Turek, Physical properties of tetragonal CuMnAs: A first-principles study, *Phys. Rev. B* **96**, 094406 (2017).
- [20] M. Veis, J. Minár, G. Steciuk, L. Palatinus, C. Rinaldi, M. Cantoni, D. Kriegner, K. K. Tikuišis, J. Hamrle, M. Zahradník, R. Antoš, J. Železný, L. Šmejkal, X. Marti, P. Wadley, R. P. Champion, C. Frontera, K. Uhlířová, T. Duchon, P. Kužel *et al.*, Band structure of CuMnAs probed by optical and photoemission spectroscopy, *Phys. Rev. B* **97**, 125109 (2018).
- [21] F. Máca, J. Kudrnovský, P. Baláž, V. Drchal, K. Carva, and I. Turek, Tetragonal CuMnAs alloy: Role of defects, *J. Magn. Mater.* **474**, 467 (2019).
- [22] K. Uhlířová, E. Duverger-Nédellec, R. H. Colman, J. Volný, B. Vondráčková, and K. Carva, The stability and physical properties of the tetragonal phase of bulk CuMnAs antiferromagnet, *J. Alloys Compd.* **771**, 680 (2018).
- [23] J. Volný, D. Wagenknecht, J. Železný, P. Hrcuba, E. Duverger-Nedellec, R. H. Colman, J. Kudrnovský, I. Turek, K. Uhlířová, and K. Výborný, Electrical transport properties of bulk tetragonal CuMnAs, *Phys. Rev. Materials* **4**, 064403 (2020).
- [24] A. A. Sapozhnik, M. Filianina, S. Y. Bodnar, A. Lamirand, M. A. Mawass, Y. Skourski, H. J. Elmers, H. Zabel, M. Kläui, and M. Jourdan, Direct imaging of antiferromagnetic domains in Mn<sub>2</sub>Au manipulated by high magnetic fields, *Phys. Rev. B* **97**, 134429 (2018).
- [25] M. M. Odashima, A. Marmodoro, P. Buczek, A. Ernst, and L. Sandratskii, Chirality dependent magnon lifetime in a compensated half-metallic ferrimagnet, *Phys. Rev. B* **87**, 174420 (2013).
- [26] Y. Kajiwara, K. Harii, S. Takahashi, J. Ohe, K. Uchida, M. Mizuguchi, H. Umezawa, H. Kawai, K. Ando, K. Takanashi, S. Maekawa, and E. Saitoh, Transmission of electrical signals by spin-wave interconversion in a magnetic insulator, *Nature (London)* **464**, 262 (2010).
- [27] L. J. Cornelissen, J. Liu, R. A. Duine, J. B. Youssef, and B. J. van Wees, Long-distance transport of magnon spin information in a magnetic insulator at room temperature, *Nat. Phys.* **11**, 1022 (2015).
- [28] T. Jungwirth, V. Novák, X. Martí, M. Cukr, F. Máca, A. B. Shick, J. Mašek, P. Horodyská, P. Němec, V. Holý, J. Zemek, P. Kužel, I. Němec, B. L. Gallagher, R. P. Champion, C. T. Foxon, and J. Wunderlich, Demonstration of molecular beam epitaxy and a semiconducting band structure for I-Mn-V compounds, *Phys. Rev. B* **83**, 035321 (2011).
- [29] P. Wadley, V. Novák, R. P. Champion, C. Rinaldi, X. Martí, H. Reichlová, J. Železný, J. Gazquez, M. A. Roldan, M. Varela, D. Khalyavin, S. Langridge, D. Kriegner, F. Máca, J. Mašek, R. Bertacco, V. Holý, A. W. Rushforth, K. W. Edmonds, B. L. Gallagher *et al.*, Tetragonal phase of epitaxial room-temperature antiferromagnet CuMnAs, *Nat. Commun.* **4**, 2322 (2013).
- [30] V. Hills, P. Wadley, R. P. Champion, V. Novak, R. Beardsley, K. W. Edmonds, B. L. Gallagher, B. Ouladdiaf, and T. Jungwirth, Paramagnetic to antiferromagnetic transition in epitaxial tetragonal CuMnAs, *J. Appl. Phys.* **117**, 172608 (2015).
- [31] L. Linowsky and W. Bronger, Synthese und Kristallstruktur von KMnP und KMnAs, *ZAAC J. Inorg. Gen. Chem.* **409**, 221 (1974).
- [32] H.-U. Schuster and G. Achenbach, Ternaere Verbindungen des Natriums und Kaliums mit Mangan und Elementen der 5. Hauptgruppe, *Z. Naturforsch. B* **33**, 113 (1978).

- [33] G. Achenbach and H.-U. Schuster, Ternäre Verbindungen des Lithiums und Natriums mit Mangan und Elementen der 5. Hauptgruppe, *Z. Anorg. Allg. Chem.* **475**, 9 (1981).
- [34] W. Bronger, P. Müller, R. Höppner, and H.-U. Schuster, The Magnetic-properties of NaMnP, NaMnAs, NaMnSb, NaMnBi, LiMnAs, and KMnAs, characterized by neutron-diffraction Experiments, *ZAAC J. Inorg. Gen. Chem.* **539**, 175 (1986).
- [35] W. Zhou, S. Wu, and S. Li, First-principles study of the magnetic and electronic properties of AMnAs (A=Li, Na, K, Rb, Cs), *J. Magn. Magn. Mater.* **420**, 19 (2016).
- [36] A. Beleanu, J. Kiss, G. Kreiner, C. Köhler, L. Mächler, W. Schnelle, U. Burkhardt, S. Chadov, S. Medvediev, D. Ebke, C. Felser, G. Cordier, B. Albert, A. Hoser, F. Bernardi, T. I. Larkin, D. Pröpper, A. V. Boris, and B. Keimer, Large resistivity change and phase transition in the antiferromagnetic semiconductors LiMnAs and LaOMnAs, *Phys. Rev. B* **88**, 184429 (2013).
- [37] A. Beleanu, Ternary lithium based compounds used for technological applications, Ph.D. thesis, Mainz University, 2014.
- [38] J. Yang, A. Wegner, C. M. Brown, and D. Louca, Defect-driven extreme magnetoresistance in an I-Mn-V semiconductor, *Appl. Phys. Lett.* **113**, 122105 (2018).
- [39] A. Wegner, D. Louca, K. M. Taddei, and J. Neufeind, Charge density modulation and defect ordering in the  $\text{Na}_x\text{MnBi}_y$  magnetic semimetal, *Phys. Rev. B* **102**, 020403(R) (2020).
- [40] K. Uhlířová, R. Tarasenko, F. J. Martínez-Casado, B. Vondráčková, and Z. Matěj, Synthesis and single crystal study of  $\text{CuMn}_3\text{As}_2$  and  $\text{Cu}_2\text{Mn}_4\text{As}_3$ , *J. Alloys Compd.* **650**, 224 (2015).
- [41] See Supplemental Material at <http://link.aps.org/supplemental/10.1103/PhysRevB.105.125204> for details about the sample preparation and used computational convention.
- [42] V. Petříček, M. Dušek, and L. Palatinus, Crystallographic computing system JANA2006: General features, *Z. Kristallogr.* **229**, 345 (2014).
- [43] H. W. Nesbitt and D. Banerjee, Interpretation of XPS Mn(2p) spectra of Mn oxyhydroxides and constraints on the mechanism of MnO<sub>2</sub> precipitation, *American Mineralogist* **83**, 305 (1984)
- [44] P. Wernet, B. Sonntag, M. Martins, P. Glatzel, B. Obst, and P. Zimmermann, Multiplet splitting and valence-shell recoupling in the core-level 2p photoelectron spectrum of atomic mn and of mn compounds, *Phys. Rev. A* **63**, 050702(R) (2001).
- [45] R. Tarasenko, M. Vališka, M. Vondráček, K. Horáková, V. Tkáč, K. Carva, P. Baláž, V. Holý, G. Springholz, V. Sechovský, and J. Honolka, Magnetic and structural properties of Mn-doped  $\text{Bi}_2\text{Se}_3$  topological insulators, *Physica B* **481**, 262 (2016).
- [46] M. Taguchi, T. Uozumi, K. Okada, H. Ogasawara, and A. Kotani, Atomic Many-Body Effects for the p-Shell Photoelectron Spectra of Transition Metals, *Phys. Rev. Lett.* **86**, 3692 (2001).
- [47] A. Hariki, T. Uozumi, and J. Kuneš, LDA+DMFT approach to core-level spectroscopy: Application to 3d transition metal compounds, *Phys. Rev. B* **96**, 045111 (2017).
- [48] M. Taguchi, T. Uozumi, and A. Kotani, Theory of x-ray photoemission and x-ray emission spectra in Mn compounds, *J. Phys. Soc. Jpn.* **66**, 247 (1997).
- [49] P. S. Bagus and E. S. Ilton, Effects of covalency on the p-shell photoemission of transition metals MnO, *Phys. Rev. B* **73**, 155110 (2006).
- [50] E. A. Kraut, R. W. Grant, J. R. Waldrop, and S. P. Kowalczyk, Precise Determination of the Valence-band edge in x-ray Photoemission Spectra: Application to Measurement of Semiconductor Interface Potentials, *Phys. Rev. Lett.* **44**, 1620 (1980).
- [51] Y. Koshkid'ko, E. Dilmeva, J. Cwik, K. Rogacki, D. Kowalska, A. Kamantsev, V. Koledov, A. Mashirov, V. Shavrov, V. Valkov, A. Golovchan, A. Sivachenko, S. Shevrytalov, V. Rodionova, I. Shchetinin, and V. Sampath, Giant reversible adiabatic temperature change and isothermal heat transfer of MnAs single crystals studied by direct method in high magnetic fields, *J. Alloys Compd.* **798**, 810 (2019).
- [52] A. de Campos, M. Mota, S. Gama, A. Coelho, B. White, M. da Luz, and J. Neumeier, Single crystal growth and characterization of MnAs, *J. Cryst. Growth* **333**, 54 (2011).
- [53] A. Carvalho, A. Coelho, S. Gama, F. Gandra, P. Ranke, and N. De Oliveira, Erratum to: Investigation of the first-order metamagnetic transitions and the colossal magnetocaloric effect using a Landau expansion applied to MnAs compound, *Eur. Phys. J. B* **78**, 137 (2010).
- [54] R. O. Jones and O. Gunnarsson, The density functional formalism, its applications and prospects, *Rev. Mod. Phys.* **61**, 689(1989).
- [55] H. Ebert, D. Ködderitzsch, and J. Minár, Calculating condensed matter properties using the KKR-Green's function method-recent developments and applications, *Rep. Prog. Phys.* **74**, 096501 (2011).
- [56] H. Ebert, The Munich SPR-KKR package, <https://www.ebert.cup.uni-muenchen.de/sprkk>.
- [57] A. I. Liechtenstein, M. I. Katsnelson, and V. A. Gubanov, Exchange interactions and spin-wave stiffness in ferromagnetic metals, *J. Phys. F: Met. Phys* **14**, L125 (1984).
- [58] Authors of Ref. [35] use a different approach to estimate the stability of magnetic order: Instead of calculating the  $J_{ij}$  parameters as in our paper, they compare the total energy in the ferromagnetic and AFM state. We comment on this approach in the Appendix.
- [59] O. Eriksson, A. Bergman, L. Bergqvist, and J. Hellsvik, *Atomistic Spin-Dynamics*, 1st ed. (Oxford University Press, Uppsala, 2017).
- [60] J. Hellsvik, D. Thonig, K. Modin, D. Iusan, A. Bergman, O. Eriksson, L. Bergqvist, and A. Delin, General method for atomistic spin-lattice dynamics with first-principles accuracy, *Phys. Rev. B* **99**, 104302 (2019).
- [61] M. Wang, R. A. Marshall, K. W. Edmonds, A. W. Rushforth, R. P. Campion, and B. L. Gallagher, Three-dimensional Heisenberg critical behavior in the highly disordered dilute ferromagnetic semiconductor (Ga,Mn)As, *Phys. Rev. B* **93**, 184417 (2016).
- [62] B. I. Halperin, On the Hohenberg-Mermin-Wagner theorem and its limitations, *J. Stat. Phys.* **175**, 521 (2019).
- [63] X.-Y. Li, F. Lou, X.-G. Gong, and H. Xiang, Constructing realistic effective spin hamiltonians with machine learning approaches, *New J. Phys.* **22**, 053036 (2020).
- [64] G. Fischer, M. Däne, A. Ernst, P. Bruno, M. Lüders, Z. Szotek, W. Temmerman, and W. Hergert, Exchange coupling in transition metal monoxides: Electronic structure calculations, *Phys. Rev. B* **80**, 014408 (2009).
- [65] P. Lloyd and P. Smith, Multiple scattering theory in condensed materials, *Adv. Phys.* **21**, 69 (1972).
- [66] V. P. Antropov, B. N. Harmon, and A.N. Smirnov, Aspects of spin dynamics and magnetic interactions, *J. Magn. Magn. Mater.* **200**, 148 (1999).